Eidgenössische Technische Hochschule Zürich
Swiss Federal Institute of Technology Zurich

Ho June Kim

Assembly and characterization of compact double-pass AOM board

Semester Thesis

as part of Master's Degree in Quantum Engineering at ETH Zurich
Ion Trap Quantum Computing Group
Paul Scherrer Institute

Supervision

Julian Schmidt
Prof. Jonathan Home

January 10, 2024

Abstract

Double-pass acousto-optic modulator (AOM) systems are widely used in many trapped atom experiments. In this semester thesis, results from assembly and characterization of compact fiber-in fiber-out double-pass AOM board for $\lambda = 397$ nm are reported. First, the AOM to be used for the double-pass system was tested by itself in a separate single-pass set-up. Then, peak efficiency of 36 % with effective 3-dB bandwidth of 200 MHz and extinction ratio of > 70 dB were measured for the assembled double-pass board. Finally, the board was tested for both stability under temperature cycling and long term drift under ambient lab temperatures. Throughout the project some minor errors and improvements in the design were noted, and a procedure was developed for rapid assembly of the multiple identical boards in the future. The double-pass system is presented here as a solution to poor scalability of breadboard systems, all the while maintaining the performance not yet available in fiber-coupled AOMs.

Acknowledgements

I would like to thank my supervisor Julian Schmidt for his technical guidance and patience throughout the project. I would also like to thank the rest of Ion Trap Quantum Computing group members for their hospitality during my frequent visits to the lab at Paul Scherrer Institute.

Contents

Chapter 1

Introduction

Acousto-optic modulator (AOM) is a device which can change the amplitude, frequency, and phase of an input laser beam via interaction with an acoustic wave. AOMs are widely used in many trapped atom experiments where multiple lasers are shone on the ions to cool their mechanical motion and to manipulate and read-out the internal states of the ions. AOMs in such experiments are often used in a "double-pass configuration", where the light is passed twice through the AOM to increase the frequency tunability and the extinction ratio (1).

Number of double-passed AOMs required in trapped-ion experiments are increasing as the number of independently addressed qubits across various hardware platforms are increasing in the push for scalable quantum processors. Traditionally, double-passed AOM systems are built on optical breadboards which can be bulky and therefore scales poorly as experiments push towards more and more qubits. On the other hand, commercially available fiber-coupled AOMs are compact in size, but to date still lack in performance compared to the breadboard set-ups, especially in extinction ratio which is crucial for trapped-ion experiments. During the semester project, a compact and modular double-pass AOM system based on custom-machined board was built and characterized as an intermediate solution which improves scalability without as much sacrifice in performance.

The thesis is organized as follows. In chapter 2, the underlying theory behind acousto-optics is presented, as well as an introduction to double-pass configuration and its usage in experiments with trapped $^{40}Ca^{+}$ ions. In chapter 3, results from single-pass testing are presented, which was done to characterize the AOM itself separate from rest of the double-pass system. Finally in chapter 4, characterizations of double-pass board are discussed, along with procedure for rapid assembly of multiple boards.

Chapter 2

Acousto-optic modulators

In this chapter, basics of AOM, double-pass configuration and their uses in experiments with $^{40}Ca^{+}$ ions are introduced. Analysis of AOM operation using acousto-optics theory is also presented, including derivation of AOM responses to RF frequency and power, which were measured in lab and are presented in chapter 3.

2.1 Basics of acousto-optic moodulators

Two main components of an AOM are a crystal that mediates the interaction between the input light and acoustic wave travelling through the crystal, and a transducer attached to the crystal which converts the RF electrical signal into mechanical oscillation and generates the acoustic wave. The other end of the crystal is usually cut at an angle to reflect the acoustic wave away from the light to prevent reflected wave going through the interaction again. Otherwise, the crystal is terminated with an acoustic wave absorber to also prevent any reflections. It is also quite common for AOMs to come with an impedance matching circuit to maximize the RF power absorbed by the crystal at the desired RF center frequency.

As monochromatic beam of light traverses the crystal, the acousto-optic interaction diffracts the light into discrete beams with different deflection angles with respect to the original beam, each corresponding to a different "order" of diffraction. One can maximize the intensity of one of the diffraction orders by adjusting the incident angle of the input beam. The optimal incidence angle is called the Bragg angle θ_B.

Heuristically this phenomenon could be understood as a consequence of a photon-phonon interaction inside the crystal of the AOM (1); after photon with energy $\hbar\omega$ interacts with discrete phonons each with energy $\hbar\Omega$, where ω and Ω are angular fre-

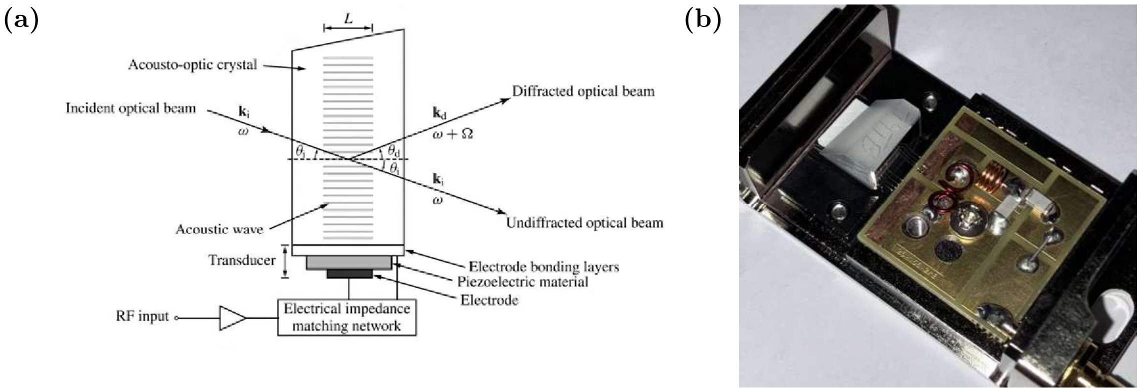

Figure 2.1: (a) Schematic of an AOM. Transducer generates a travelling acoustic wave in the crystal. The RF port is impedance matched around some center frequency using a matching network. The arrows show the directions of incident optical beam and different diffraction orders. Taken from (3). (b) Picture of the AOM used for measurement with the top cover removed. Golden cylinder by the bottom right corner (slightly cropped in image) is the SMB connector where the RF cable can be connected to. Connected to the connector is presumably the matching network and circuits for the transducer. Crystal (crystal quartz) with the angled cut is also shown.

quencies of optical and acoustic waves respectively, photon's energy can be changed to $\hbar(\omega + q\Omega)$, where q is the diffraction order, $q \in \mathbb{Z}$. To maximize the intensity of order q, you have to adjust the incidence angle to $\theta = \theta_B$ such that the momentum conservation of photon is satisfied. From the diagram, one can easily see that $\sin\theta = q\Omega/(2\omega) = qf_{RF}\lambda_o n/(2c)$, where f_{RF} is the RF frequency, λ_o is the optical wavelength, n is the refractive index of the crystal.

2.2 Acousto-optics theory

Most of the material covered in this section follows the theoretical treatment from Optical Electronics by Ghatak (2) and Photonic Devices by Liu (3). The analysis is limited to isotropic medium for simplicity.

2.2.1 Photoelastic coefficients

Acousto-optic diffractions in AOMs are based on photoelastic effect, a phenomenon where mechanical strain in the medium changes the optical properties. Photoelastic effect in isotropic medium is characterized by a rank-4 tensor of photoelastic coefficients p_{ijkl} and the change in optical properties due to mechanical strain is defined by the expression below:

$$\eta_{ij}(S) = \eta_{ij} + \Delta\eta_{ij}(S) = \eta_{ij} + \sum_{k,l} p_{ijkl} S_{kl} \tag{2.1}$$

where $\eta = \epsilon_0/\epsilon$ is the rank-2 permeability tensor, S is the rank-2 strain tensor, and indices *i, j, k, l* run from 1 to 3 and represent the 3 spatial axes.

Due to symmetry of the strain tensor, indices *i,j* and *k,l* can be combined to indices α and β which run from 1 to 6, such that:

$$\begin{aligned} &\alpha = 1 \rightarrow (i,j) = (1,1) && \alpha = 2 \rightarrow (i,j) = (2,2) \\ &\alpha = 3 \rightarrow (i,j) = (3,3) && \alpha = 4 \rightarrow (i,j) = (2,3),(3,2) \\ &\alpha = 5 \rightarrow (i,j) = (3,1),(1,3) && \alpha = 6 \rightarrow (i,j) = (1,2),(2,3) \end{aligned} \tag{2.2}$$

and similar rule applies to β and *k,l.*

Then, equation 2.1 is modified to:

$$\eta_{\alpha}(S) = \eta_{\alpha} + \Delta\eta_{\alpha}(S) = \eta_{\alpha} + \sum_{\beta} p_{\alpha\beta} S_{\beta} \tag{2.3}$$

In this index convention, the photoelastic tensor for isotropic medium has the following form:

$$\begin{bmatrix} p_{11} & p_{12} & p_{12} & 0 & 0 & 0 \\ p_{12} & p_{11} & p_{12} & 0 & 0 & 0 \\ p_{12} & p_{12} & p_{11} & 0 & 0 & 0 \\ 0 & 0 & 0 & \frac{1}{2}(p_{11} - p_{12}) & 0 & 0 \\ 0 & 0 & 0 & 0 & \frac{1}{2}(p_{11} - p_{12}) & 0 \\ 0 & 0 & 0 & 0 & 0 & \frac{1}{2}(p_{11} - p_{12}) \end{bmatrix} \tag{2.4}$$

Photoelastic tensor for isotropic medium has two degrees of freedom, p_{11} and p_{12}. Note that even for isotropic medium, photoelastic tensor itself is not necessarily isotropic.

Photoelastic coefficients describe the change in permeability by convention. To convert the permeability tensor to a more familiar permittivity tensor ϵ, one can take the differential of the relation $\epsilon\eta = \epsilon_0$ to derive the following:

$$\Delta\epsilon_{ij} = -\epsilon_0 n_i^2 n_j^2 \Delta\eta_{ij} \tag{2.5}$$

using the index convention in eq. 2.1

2.2.2 Coupled wave equations

To derive the expression for diffracted electric fields, we start with the wave equation for electric field:

$$\vec{\nabla}^2 \vec{E} = \mu_0 \frac{\partial^2 \vec{E}}{\partial t^2} = \mu_0 \frac{\partial^2}{\partial t^2}[\epsilon_u + \Delta\epsilon sin(\Omega t - Kz)]\vec{E} \tag{2.6}$$

where Ω and K are frequency and wavenumber of acoustic wave, ϵ_u is the unperturbed permittivity tensor. Propagation of acoustic wave is in $+z$ direction. Since optical frequency is much larger than the acoustic frequency,

$$\vec{\nabla}^2 \vec{E} \approx \mu_0[\epsilon_u + \Delta\epsilon sin(\Omega t - Kz)]\frac{\partial^2 \vec{E}}{\partial t^2} \tag{2.7}$$

Now if one plugs in $E \propto e^{i\omega t}$ into eq. 2.7, where ω denotes the optical frequency, terms proportional to $e^{i\omega t}$ as well as $e^{i(\omega \pm \Omega)t}$ appear on the right hand side of the equation. A rigorous ansatz for solution to eq. 2.7 would be an infinite sum of terms with each term proportional to $e^{i(\omega \pm q\Omega)t}$ where q runs from 0 to infinity, however, for simplicity we limit the ansatz to $\vec{E} = \vec{E_0} + \vec{E_+} + \vec{E_-}$ where:

$$\vec{E_i} = \hat{e_i} A_i e^{i(\omega_i t - \alpha_i x - \beta_i z)} \tag{2.8}$$

where α_i is the x component and β_i the z component of the optical wavevector k_i, $\omega_i = \omega$ for i = 0 and $\omega \pm \Omega$ for i = $\pm$, and $\hat{e_i}$ is the unit polarization vector.

Now we make the following approximations. First, we assume that A_i's are slow varying amplitudes, and therefore we can neglect the second derivatives of A_i's. Second, we assume small Bragg angle θ_B; input light travels almost parallel to $+x$ axis, so we can neglect the derivative of A_i's with respect to z and y, i.e. the amplitude only varies in x axis. Applying these approximations and equating terms with same time dependence, we get the following coupled equations:

$$\begin{aligned} -2i\alpha_0 \frac{dA_0}{dx} e^{-i(\alpha_0 x + \beta_0 z)} &= -\frac{1}{2i}\mu_0 \omega^2 \Delta\epsilon_\pm (-A_+ e^{-i(\alpha_+ x + (\beta_+ - K)z)} + A_- e^{-i(\alpha_- x + (\beta_- + K)z)}) \\ -2i\alpha_\pm \frac{dA_\pm}{dx} e^{-i(\alpha_\pm x + \beta_\pm z)} &= \mp \frac{1}{2i}\mu_0 \omega^2 \Delta\epsilon_\pm (-A_0 e^{-i(\alpha_0 x + (\beta_0 \pm K)z)}) \end{aligned} \tag{2.9}$$

where $\Delta\epsilon_\pm = \hat{e}_\pm \Delta\epsilon \hat{e}_0$.

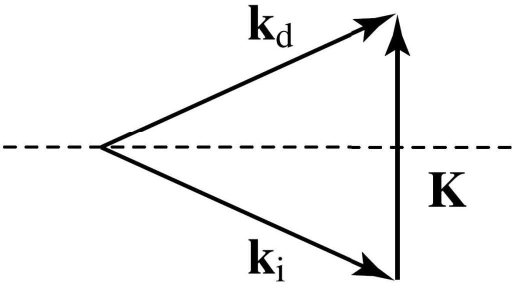

Figure 2.2: Phase-matching diagram showing wavevectors of incident and first-order deflected beams. In the figure, k_+ is written as k_d and k_0 as k_i. Taken from (3).

The z-dependent factors should be cancelled out, so $\beta_\pm = \beta_0 \pm K$. Here, the wavevectors of ± 1 diffraction orders are forced to follow momentum conservation. The above expression also tells us that $+1$ and -1 orders will be deflected in opposite directions with respect to the 0-th order beam. We will also later show that $A_\pm$ is negligible if $\alpha_\pm$ is not similar to α. Only one of α_+ or α_- can be equal to α_0 with fixed angle; this can be understood graphically with phase-matching diagram of wavevectors. Since $\omega \gg \Omega$, $k_\pm \approx k_0$. If the incidence angle is such that $\alpha_+ = \alpha_0$ as shown above, k_-, which will be deflected in the opposite direction, cannot have a same x-component as k_0.

Keeping only the first order diffraction term, we get:

$$\begin{aligned} \frac{d\tilde{A}_0}{dx} &= \kappa \tilde{A}_+ e^{ix\Delta\alpha} \\ \frac{d\tilde{A}_+}{dx} &= -\kappa \tilde{A}_0 e^{-ix\Delta\alpha} \end{aligned} \tag{2.10}$$

where $\kappa = \frac{\omega^2 \mu_0 \Delta\epsilon_+}{4\sqrt{\alpha_0 \alpha_+}}$, $\delta = \sqrt{\kappa^2 + \frac{1}{4}(\Delta\alpha)^2}$, and $\Delta\alpha = \alpha_0 - \alpha_+$ is the difference in x-component of the wavevectors which we will call "phase mismatch", and $\tilde{A}_i = \sqrt{\frac{\alpha_i}{2\omega_i \mu_0}}$ is the normalized amplitude such that the electric field intensity $I = |\tilde{A}|^2$.

The above coupled equations have the following solution:

$$\begin{aligned} \tilde{A}_0(x) &= C_0 e^{ix(\frac{1}{2}\Delta\alpha + \delta)} + D_0 e^{ix(\frac{1}{2}\Delta\alpha - \delta)} \\ \tilde{A}_+(x) &= (C_+ e^{ix(\frac{1}{2}\Delta\alpha + \delta)} + D_+ e^{ix(\frac{1}{2}\Delta\alpha - \delta)}) e^{-ix\Delta\alpha} \end{aligned} \tag{2.11}$$

where C_0, D_0 are complex coefficients, and $C_+ = \frac{i}{\kappa}(\frac{1}{2}\Delta\alpha + \delta)C_0$, $D_+ = \frac{i}{\kappa}(\frac{1}{2}\Delta\alpha - \delta)D_0$. Since at input there is only 0-th order light, we can impose boundary condi-

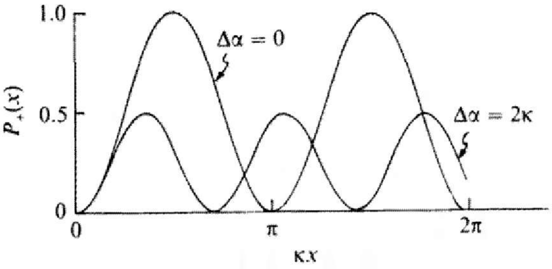

Figure 2.3: Plot of eq. 2.12. ($P_+ = \eta$) Note that when phase mismatch is 0, diffraction can reach perfect efficiency, and as the phase mismatch increases, the efficiency is attenuated. Taken from (2).

tions $\tilde{A}_0(x=0) = 1$ and $\tilde{A}_+(x=0) = 0$ to find:

$$\eta(x) = |\tilde{A}_+(x)|^2 = \left(\frac{\kappa}{\delta}\right)^2 \sin^2(\delta x) \tag{2.12}$$

where η is the first order diffraction efficiency.

Plotting eq. 2.12 for different phase mismatch $\Delta\alpha$, we see that the first order power attenuates with increasing phase mismatch, which justifies ignoring the -1 order to get eq. 2.10. We also see from eq. 2.12 that η depends on κ which is proportional to $\Delta\epsilon_+$, which means polarization of the beam can affect the efficiency even for isotropic media.

2.2.3 RF frequency and power responses

Substituting $x = L$, where L is the length of the transducer, we get

$$\eta = \frac{1}{\sqrt{1 + (\frac{\Delta\alpha}{2\kappa})^2}} \sin^2\left(\kappa L \sqrt{1 + \left(\frac{\Delta\alpha}{2\kappa}\right)^2}\right) \tag{2.13}$$

From the geometry of the problem, phase mismatch term $\Delta\alpha$ can be calculated as follows:

$$\Delta\alpha(f) = \sqrt{k^2 - \frac{(2\pi f_c/v_a)^2}{4}} - \sqrt{k^2 - \frac{(2\pi f/v_a)^2}{4}} \tag{2.14}$$

where f_c is the center frequency of the AOM. The wavenumber of the diffracted wave is approximated as k above since $\omega \gg \Omega$.

κ in eq. 2.13 can be expressed in terms of RF power by finding the relationship between strain amplitude and intensity of the acoustic wave. Consider a 2D sheet of

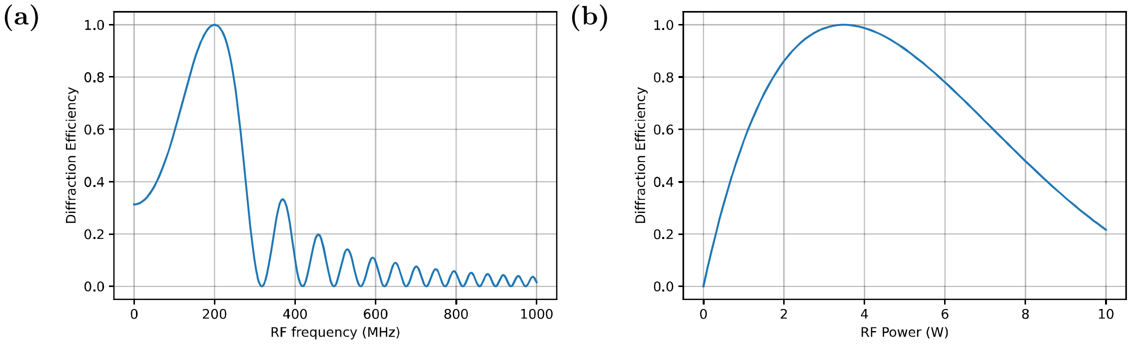

Figure 2.4: Plots from simulated RF frequency and power responses. For frequency response, eq. 2.13 was combined with eq. 2.14, and for power response, eq. 2.13 was combiend with eq. 2.17. Length and height of the transducer simulated were arbitrarily chosen to be 1.5 cm and 1 mm respectively.

atoms oscillating longitudinally as acoustic wave propagates through it. Infinitesimal kinetic energy generated by the sheet is given by:

$$dU = \frac{1}{2}dm\left(\frac{\partial u}{\partial t}\right)^2 = \frac{1}{2}\rho A dx\left(\frac{\partial u}{\partial x}\frac{\partial x}{\partial t}\right)^2 = \frac{1}{2}\rho A dx(S v_a)^2 \tag{2.15}$$

where dm is the infinitesimal mass of the atom sheet, u is the atomic displacement, ρ is the mass density, v_a is the acoustic speed and $A = L \times H$ is the area of the sheet. Then intensity of the acoustic wave generated by the sheet is given by:

$$I_a = \left(\frac{dU}{dt}\right)/A = \frac{1}{2}\rho S^2 v_a^3 \tag{2.16}$$

Eq. 2.5 in isotropic media can be written as $\Delta\epsilon_{ij} = -\epsilon_0 n^4 p S$, where p is the relevant photoelastic coefficient. In this analysis we use $p = p_{11}$ since the acoustic wave is longitudinal. Then, combining the above with eq. 2.16 and the definition of κ we get:

$$\kappa = \frac{\pi}{\lambda_o}\sqrt{\frac{n^6 p_{11}^2}{2\rho v_a^3 I_a}} \tag{2.17}$$

We can also write the above equation in terms of RF power by using $I_a = P_a/A$.

RF frequency and power responses were simulated and plotted with $\lambda_o = 397$ nm, $f_c = 200$ MHz, transducer length $L = 1.5$ cm and transducer height $H = 1$ mm. For the crystal medium, fused silica was assumed. Fused silica was chosen because of its isotropic geometry and similar optical properties to crystal quartz, which is the crystal used for the actual AOM in later chapters. For frequency response, power of

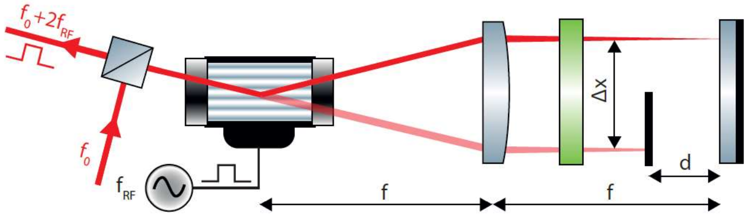

Figure 2.5: Schematic of double-pass system with polarization-based beam separation. Quarter-wave plate (green) rotates the polarization of the second-pass by 90 degrees and polarization beam splitter discriminates the beams based on polarizations. Taken from (4)

3.4 W was assumed, and for power response, frequency of 200 MHz was assumed.

In the frequency response plot, you can see the oscillations coming from $\sin^2$ with an envelope that peaks at the center frequency. For both responses, there exists an optimal frequency or power which maximizes the diffraction efficiency of the AOM. Note that the responses here do not take any RF effects into account, and is only modelling the effect of phase mismatch.

2.3 Double-pass configuration

Double-pass configuration refers to a setup where the light passes through the same AOM twice. It consists of an AOM and a cat's eye retroreflector made with lens one focal length away from the AOM and a mirror which reflects the light coming out of the AOM back in for the second time.

Double-pass configuration trades off frequency tunability for the overall efficiency. Frequency tunability is improved since now the optical frequency is shifted by twice the RF frequency, resulting in effective bandwidth which is twice as broad. The deflection angle caused by the first pass is also exactly compensated for in the second pass as the light goes back through the crystal in the opposite direction, which increases the bandwidth of fiber coupling efficiency for fiber coupled systems.

Light coming out of the second pass horizontally overlaps with the input light in double-pass systems. To discriminate the input light with the output, two different schemes are often used. First is polarization separation, where polarization beam splitter is placed before and a quarter waveplate after the AOM such that the second pass output beam has polarization orthogonal to the input beam, is filtered via the beam splitter. Second is height separation, where the input and output beams are separated vertically by height. For height separation scheme, a prism can be used instead of a flat mirror in cat's eye retroreflector such that it can change the height

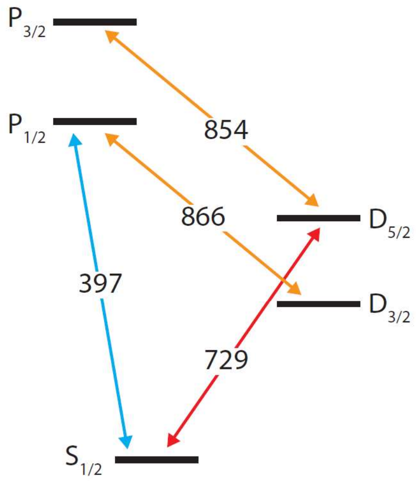

Figure 2.6: Schematic of internal states of $^{40}Ca^{+}$. There are 4 different wavelengths involved in controlling the state of the ion. Optical qubit is often encoded in $S_{1/2}$ and $D_{5/2}$ states, so extinction ratio for the 397 nm light becomes critical for long lifetime of the qubits. Taken from (4)

of the beam while reflecting the beam back to the AOM. Polarization separation is generally easier to align, however it requires more optical elements and it also introduces a different polarization for the second pass. If the change in diffraction efficiency is negligible with different polarizations, this is not an issue. However, for crystal quartz AOM used for the project, the polarization must remain vertical to the surface and for this reason height-based discrimination was chosen.

Another advantage of using a double-pass configuration comes from extinction ratios. Extinction ratio refers to the ratio between optical power at the output when the RF is turned on and off, and it is an important parameter for sensitive systems such as trapped-ion experiments. By passing the light twice, double-pass systems effectively squares the extinction ratio of single-pass, further suppressing the leakage when the RF is turned off.

The double-pass board was designed for $\lambda_o = 397$ nm and 729 nm which are used to control $^{40}Ca^{+}$ ions. Qubit is often encoded such that $|0\rangle = |D_{5/2}, m = -\frac{1}{2}\rangle$ and $|1\rangle = |S_{1/2}, m = -\frac{1}{2}\rangle$. In this project, only $\lambda_o = 397$ nm was tested. The wavelength is used to drive the transition between $S_{1/2}$ and $P_{1/2}$ which is used for 3 different stages; laser cooling, state preparation, and read-out. Frequency tunability of double-pass systems allows wider range of control for the frequency of the laser. More importantly, if some 397 nm light leaks out during the qubit manipulation / computation stage of the experiment, it can destroy the qubit information, therefore a high extinction ratio double-pass board can improve the lifetime of qubits.

Chapter 3

Single-pass characterization

The AOM to be used for double-pass board was first tested in a separate setup. The AOM used for the project is from Gooch & Housego, model number 3200-1210 (A.4). In this section, the setup and measurements from the single-pass testing are discussed.

3.1 Experimental setup

Picture of the setup used for the single-pass characterization of the AOM is shown below. Fiber collimator (S&K, 60FC-4-A4.5S-01) outcouples the light from fiber (Thorlabs, P3-375PM-FC-5) into free space. The light is then steered into the AOM with two mirrors, which allows one to tune both the incidence position and angle of the light into the AOM. Before the AOM are also a half-wave plate and a quarter-wave plate such that one can arbitrarily set the polarization of the incident light. The AOM was placed on a rotating mount which allows fine-tuning of the incidence angle to maximize the efficiency via phase-matching described in section 2.2. The modulated light is then steered with another set of two mirrors into a power sensor connected to a power meter. The power sensor is mounted with an iris diaphragm which can be adjusted along with the two mirrors to make sure that power of only the first order diffracted light is read by the power meter.

The double-pass board was also used for some of the measurements in this chapter, but without a retro-reflecting prism which reflects the light back into the AOM for the second pass. Instead, the light continues travelling off of the board, and the power sensor with iris was set up again to only measure the optical power of first order diffraction. The board as of now does not have any waveplates for polarization adjustment, so the collimator was rotated inside the collimator holder

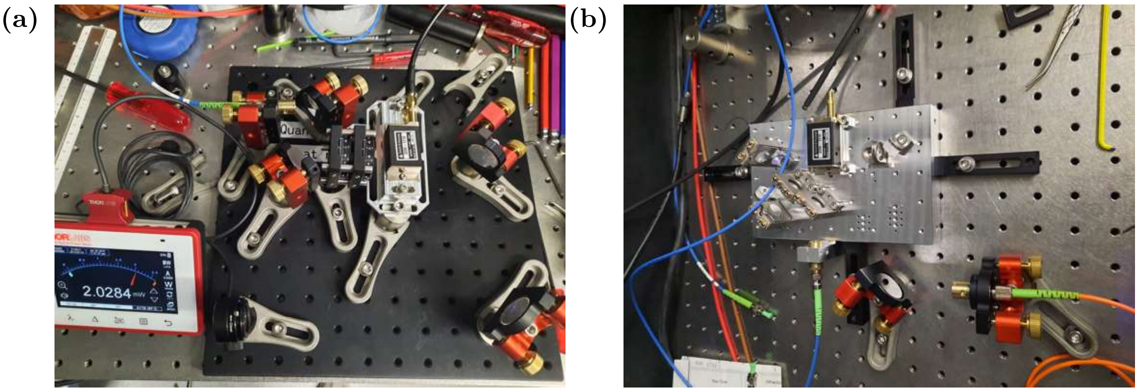

Figure 3.1: (a) Picture of the separate testing setup for single-pass. Light from fiber on the top left corner is outcoupled into free space. Quarter-wave and half-wave plates are mounted with a cage-rod system before the AOM. Power sensor with iris is located at the bottom left corner of the breadboard, which is connected to the power meter on the left. (b) Picture of the double-pass board without the cat's eye mirror. In the picture, the first order diffracted beam was then fiber coupled to calculate fiber coupling efficiency.

to maximize for diffraction efficiency.

There were two RF sources used for RF signal generation throughout the project, ARTIQ DDS and MOKU frequency synthesizer. Signals from both sources were amplified by an RF booster before going into the AOM, which has a safety mechanism that can "trip" when the output power exceeds the programmed threshold or too much power is reflected back to the output port, in which case the amplifier shuts down and no signal is outputted from it. The threshold was set to maximum rated RF power of 3.4 W or 35.4 dBm as specified in the datasheet.

3.2 Measurements

3.2.1 RF power response

First, RF amplitude was swept until maximum rated power on the datasheet of 3.4 W was reached, and diffraction efficiency was measured and plotted as a function of RF power. RF frequency was set to 200 MHz which is the center frequency of the AOM. ARTIQ DDS was used as the RF source for this measurement. (In this thesis, "diffraction efficiency" refers to "first order diffraction efficiency" unless otherwise specified.)

Typically, the diffraction efficiency saturates at an optimal RF power and as the RF power is further increased, the efficiency decreases. This was unfortunately not observed with the AOM; the efficiency continued to increase, and the RF power could

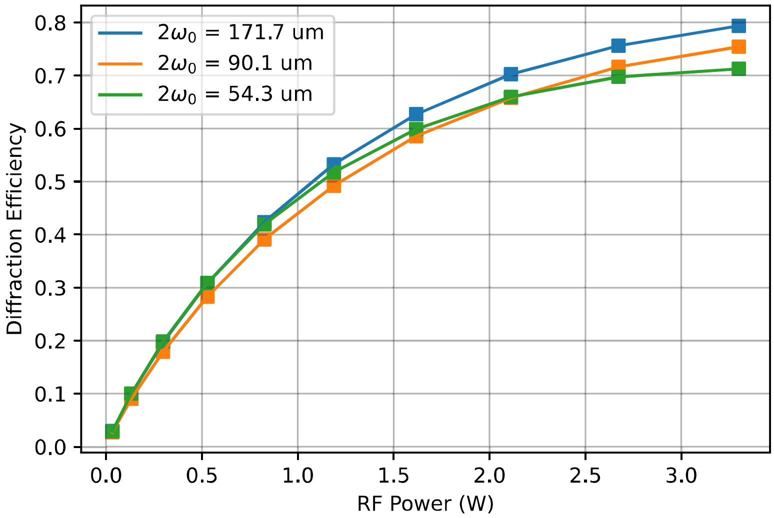

Figure 3.2: Plot of diffraction efficiency against RF power. The power response was taken for 3 different beam diameters.

not be further increased since going past the maximum rated power will damage the AOM. At RF power of 3.4 W, diffraction efficiency of 75 % at beam diameter of 90 μm was achieved.

Diffraction efficiency as a function of RF power was also measured for 2 other beam diameters by tuning the focus of the fiber collimator until desired beam diameter was reached and confirmed with a beam profiler. Beam profiler was connected to a laptop with DataRay software which extracts information about the beam such as beam diameter, centroid location, ellipticity, etc. The efficiency was measured to be higher with greater beam diameter which is the expected result.

3.2.2 RF frequency response

Next, diffraction efficiency was measured and plotted as a function of RF frequency. Two different measurements were performed for the frequency response. The first measurement was done by maximizing the efficiency for each RF frequency by tuning the mirrors and the AOM rotation mount. This amounts to finding the optimal (horizontal) incidence angle θ for each frequency. ARTIQ DDS was used as the RF source with power of 3.4 W.

According to the analysis from section 2.2, the above measurement should result in a completely flat response since the AOM is phase matched for each frequency. The variation in efficiency can be attributed to RF impedance matching and imperfect alignment. From the plot of the response, the AOM seems to be slightly more

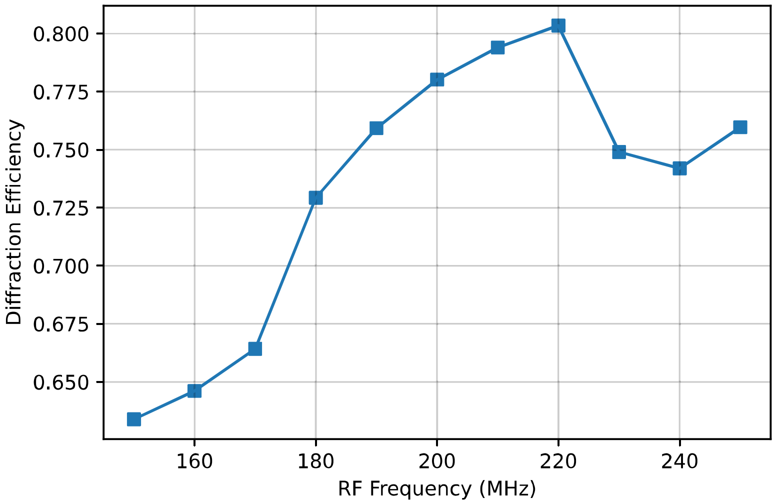

Figure 3.3: Plot of diffraction efficiency against RF frequency. For each datapoint in the plot, the beam's incidence angle was adjusted to maximize the efficiency. ($\theta \approx \theta_B$)

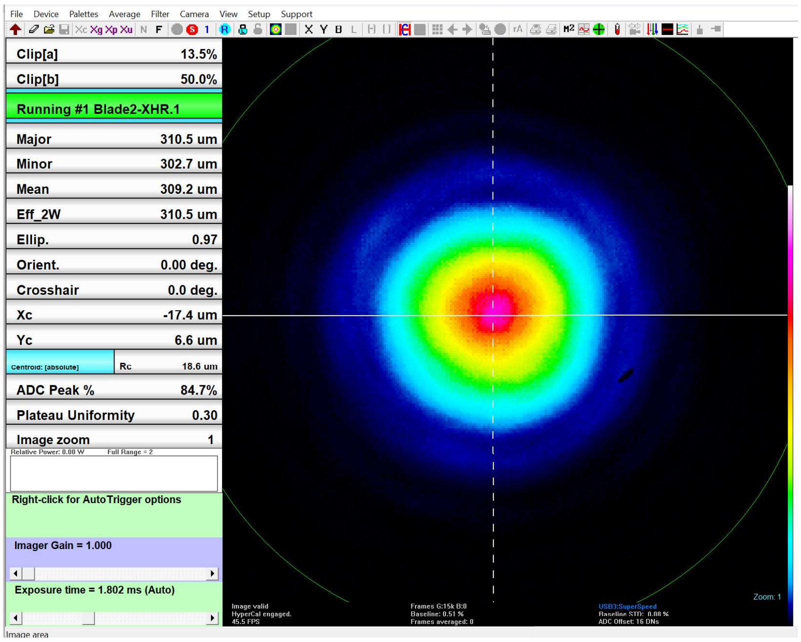

Clip[a] 13.5%
Clip[b] 50.0%
Running #1 Blade2-XHR.1
Major 310.5 um
Minor 302.7 um
Mean 309.2 um
Eff_2W 310.5 um
Ellip. 0.97
Orient. 0.00 deg.
Crosshair 0.0 deg.
Xc -17.4 um
Yc 6.6 um
Centroid: [absolute] Rc 18.6 um
ADC Peak % 84.7%
Plateau Uniformity 0.30
Image zoom 1
Relative Power: 0.00 W Full Range = 2
Right-click for AutoTrigger options
Imager Gain = 1.000
Exposure time = 1.802 ms (Auto)

Image valid
HyperCal engaged.
45.5 FPS

Frames G:15k B:0
Baseline: 0.51 %
Frames averaged: 0

USB3:SuperSpeed
Baseline STD: 0.08 %
ADC Offset: 16 DNs

Figure 3.4: Screenshot of DataRay software.

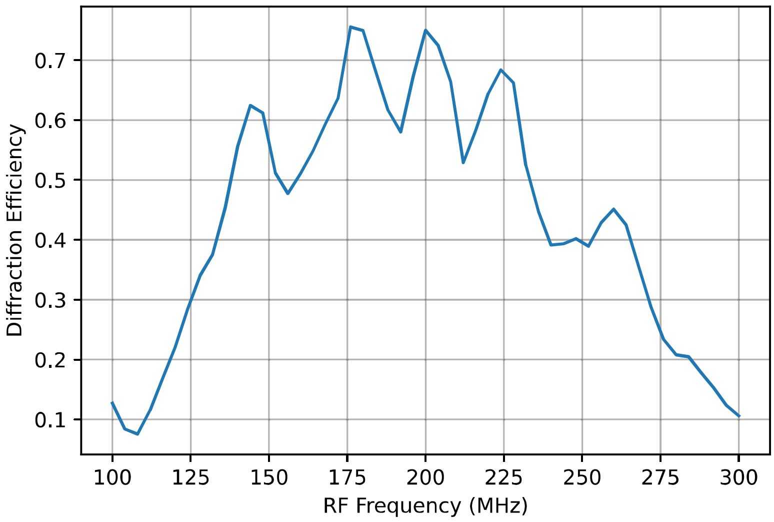

Figure 3.5: Plot of single-pass diffraction efficiency against RF frequency in free space. Unexpected peak patterns were observed during the measurement; expected frequency response is similar to the simulated plot in Chapter 2, where there is one optimal frequency where efficiency is maximum and the efficiency rolls off as you move away from the optimal frequency.

efficient at RF frequency of 220 MHz instead of 200 MHz, with diffraction efficiency of 80 %.

The second measurement was done on the double-pass board by maximizing the efficiency for center frequency of 200 MHz and sweeping the RF frequency without readjusting the incidence angle. MOKU frequency synthesizer was used for this measurement to generate the RF drive. The synthesizer comes with Python APIs which one can use to program the amplitude and frequency of the sinusoid generated. It is also integrated with a programmable oscilloscope, which was connected to an analog output port of the power meter which outputs a DC voltage proportional to the measured optical power.

The amplitude required to achieve power of 3.4 W at 200 MHz was found to be 0.47 Vpp. (with amplification from RF booster) However, as it is discussed below, this amplitude could not be used due to poor impedance matching at frequencies far away from 200 MHz, so instead RF amplitude of 0.1 Vpp was used for the frequency sweep. The plots were then re-normalized such that the diffraction efficiency at 200 MHz matches what was observed with 3.4 W from the previous section.

As discussed in the last chapter, shape of AOM's RF frequency response is similar to the power response; there exists an optimal RF frequency where the diffraction efficiency is maximum, and the efficiency should roll off smoothly as the frequency deviates from the optimal value. This was unexpectedly not observed for

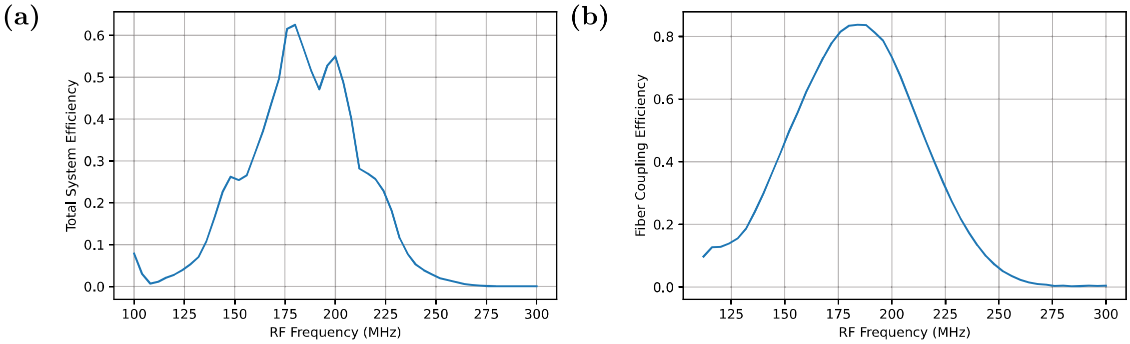

Figure 3.6: (a) Plot of RF frequency response but now the output light is fiber-coupled, so the overall efficiency is lower. (b) Response shown in (a) was divided by the free space response point-wise to get the plot of fiber coupling efficiency against RF frequency.

the second measurement, and instead, multiple peaks at different frequencies were measured as seen in the above figure.

Much effort was spent looking for the source of the multiple peaks, including changing the beam location within the aperture, polarization, beam diameter, collimation, testing multiple AOMs of the same modoel, checking for potential RF harmonics inside the AOM with a spectrum analyzer, and using a different wavelength of $\lambda = 423$ nm, but the peaks remained with little change in their locations. One potential source for the multiple peaks is imperfect absorption of acoustic waves; in theory, the acoustic wave generated by transducer should be either absorbed or reflected at the other end of the crystal such that there are no reflected acoustic waves re-interacting with the beam. Presence of such reflected waves may introduce unexpected behaviors not predicted by analysis from chapter 2. Nevertheless, diffraction efficiency of 75 % at 200 MHz was observed.

The above measurement was repeated with similar setup, where the free space power sensor was replaced with a fiber collimator that coupled the first order diffracted light into a fiber, and a fiber power sensor plugged into the power meter. This was done to see how much double-pass improves the fiber-coupling bandwidth by cancelling out the deflection angle.

Total system efficiency, combined efficiency of AOM's diffraction efficiency as well as the fiber coupling efficiency, of 55 % at 200 MHz was measured, and the system efficiency curve was divided point-wise by the free-space diffraction efficiency curve to extract the fiber coupling efficiency. Peak fiber coupling efficiency of 80 % was observed with 3-dB bandwidth of 70 MHz.

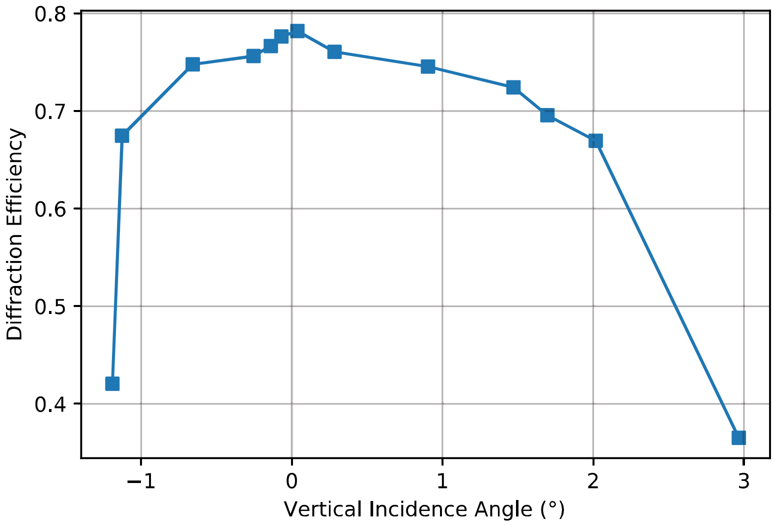

Figure 3.7: Plot of diffraction efficiency against vertical incidence angle. Diffraction efficiency is relatively flat for a range of incidence angles until it rapidly drops off.

3.2.3 Incidence angle measurement

As mentioned before, double-passed light is separated from the 0th order light via height separation where light in first and second pass vertically cross inside the AOM. Diffraction efficiency for different incidence angles were measured to make sure that the vertical angle does not play a significant role in the efficiency. To make this measurement, one of the mirrors before the AOM but closer to it was used to change the angle such that the beam position at the AOM changed as little as possible, then the mirror further away from the AOM was adjusted to maximize the efficiency such that the light was roughly crossing the center of the AOM. Then, beam profiler with DataRay was used to extract the vertical positions of the beam at different locations, which were used to calculate the angles.

From the resultant plot below, the diffraction efficiency stays more or less constant for a range of incidence angles and rapidly tapers off. The vertical angle used for the double-pass board is approximately 0.15 degrees (inverse tangent of ratio between beam radius at the D-shaped mirror and distance between D-shaped mirror and center of the AOM), which is well within the region with flat diffraction efficiencies. The asymmetry of the curve is consistent with efficiency being maximized when the light hit the AOM slightly below the center of the aperture.

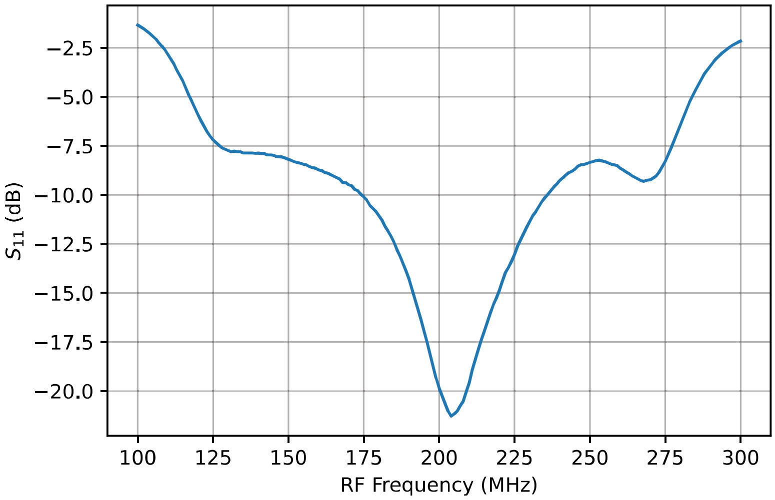

Figure 3.8: Plot of S_{11} parameter of the AOM.

3.2.4 S_{11} measurement

Finally, S_{11} parameter was measured using a FieldFox spectrum analyzer. From the plot, the AOM is well impedance-matched at 200 MHz, but for example at 100 MHz, at least 70 % of the power delivered to AOM is reflected back, which limited the RF amplitude used for frequency sweeps throughout the project. An RF circulator could be used in the future to prevent the power reflections and allow better frequency response measurements.

Chapter 4

Double-pass characterization

After the single-pass characterization, the double-pass board was assembled with the tested AOM and characterized with similar measurements from the previous chapter. The procedure used during the assembly of the board is discussed. Finally, the board was put into a temperature controlled box to test its stability under temperature cycling and long-term drift under ambident temperatures.

4.1 Experimental setup

The double-pass system again starts with a fiber collimator outcoupling the light to free space. The collimator is mounted on a custom holder mounted to the side of the board. The light is then steered by a set of two mirrors into the AOM mounted on a rotation mount. The light then goes through a lens which should parallelize light with different deflection angles. The light then goes into a retroreflector prism on a kinematic mount where the light is reflected back into the AOM for the second-pass. Once the light goes through the AOM the second time, it is met with yet another set of two mirrors and finally is coupled back into a fiber through an output fiber collimator.

The system is based on height separation scheme, so input collimator is positioned vertically below the output, and the mirrors for first pass before the AOM gives the light an upward tilt. The first pass light is then reflected twice inside the triangular prism such that the second pass light starts below the first pass and also with an upwards tilt. One of the first pass mirrors is a D-shaped mirror, which allows the second pass light to pass over it towards the first second pass mirror.

The board was designed such that the opitcal path length of first and second passes are equal, which allows for symmetric design. The board has M4 holes for

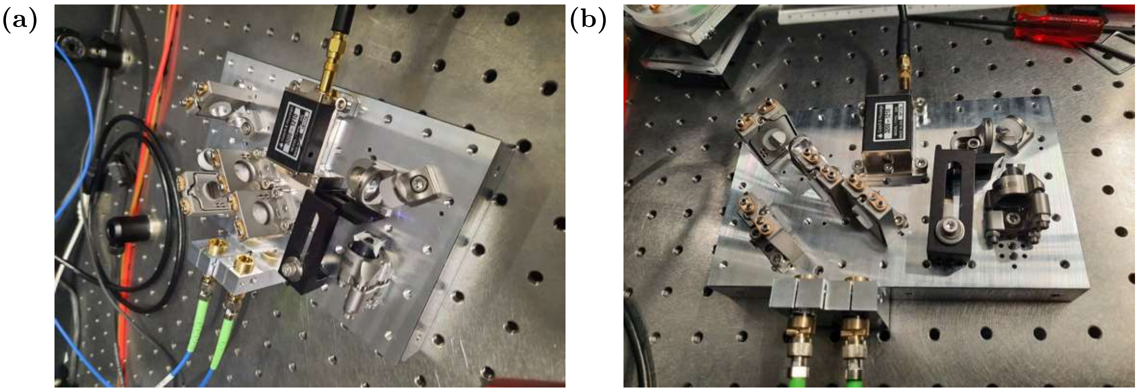

Figure 4.1: Pictures of fully-assembled double-pass board taken at different angles.

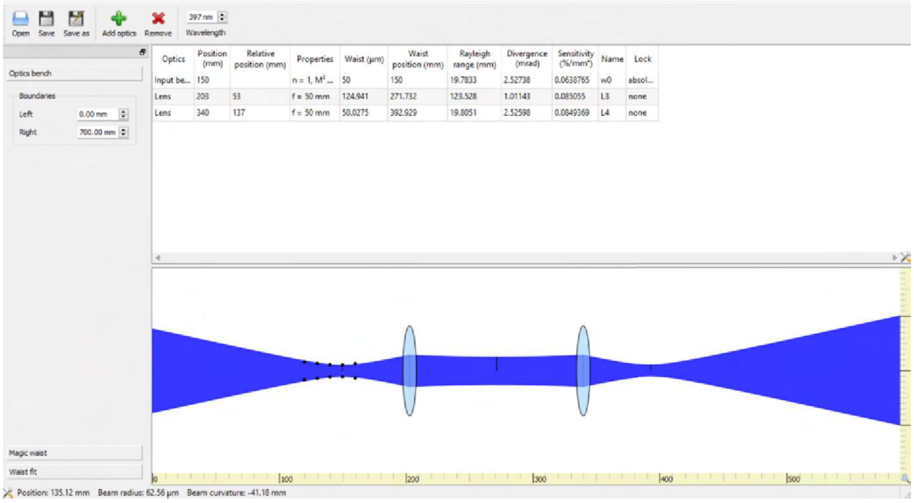

Wavelength: 397 nm

Optics bench

Boundaries

Left: 0.00 mm

Right: 700.00 mm

Optics	Position (mm)	Relative position (mm)	Properties	Waist (µm)	Waist position (mm)	Rayleigh range (mm)	Divergence (mrad)	Sensitivity (%/mm²)	Name	Lock
Input be...	150		n = 1, M² ...	50	150	19.7833	2.52738	0.0638765	w0	absol...
Lens	203	53	f = 50 mm	124.941	271.732	123.528	1.01143	0.085055	L3	none
Lens	340	137	f = 50 mm	50.0275	392.929	19.8051	2.52598	0.0849369	L4	none

Position: 135.12 mm Beam radius: 62.56 µm Beam curvature: -41.18 mm

Figure 4.2: Screenshot of GaussianBeam file for the double-pass system. Input waist was defined by beam waist size and position extracted using a separate Python script. Lens position can be changed to see how the beam diameter changes along the beam path.

mounting all the different optical components, with holes for alignment pins for precise orientations. The board has mounting holes for two different optical paths; they were designed to work for lens with focal length $f = 40$ mm for one path and $f = 50$ mm for the other, but for this project $f = 50$ mm was used for reasons mentioned below. The board and other custom parts such as the housing for the board, collimator holders, and the rotation mount were designed by Julian Schmidt and machined in the ETH Mechanical Workshop.

GaussianBeam software was used to simulate the beam diameter at different points along the beam path. The software also allows you to define the input beam and place lenses with different focal lengths at different positions along the beam path and simulate how the lenses change the beam diameter variation. The mode field diameter of fibers used in the setup was unknown, so to define the input beam,

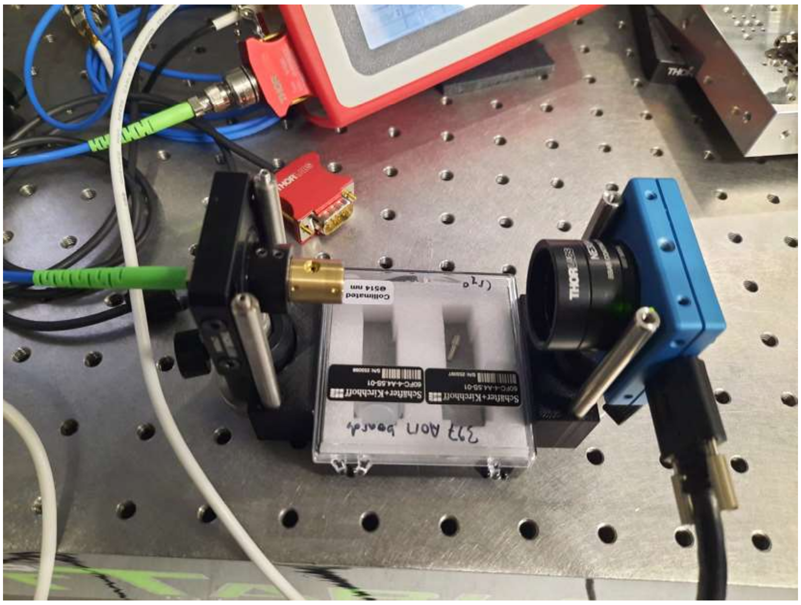

Figure 4.3: Example usage of the 3D holder. Thorlabs posts can be pressed against flat surfaces using the holder. The cage rods inserted into the holder fixes the rotation of whatever the post is mounting (beam profiler, cage mounts, etc.)

beam diameter of the input beam was measured at multiple distances away from the collimator using the 3D-printed post holders, and beam waist distance and diameter was extracted using a least-squares fit in Python. Post holders were designed such that one can push the beam profiler mounted on a post against anything with a flat side; that way, distance between profiler and the fiber collimator can be set faster and more precise. Cage rods were hammered into the two holes in the post holder which lock the orientation of the profiler.

4.2 Assembly Procedure

Here is the procedure for assembling the board.

1. Using a beam profiler, adjust the focus of both input and output collimators such that the beam waist is the correct distance away from the collimators. For the current iteration of the board, distance from end of the collimator to the beam waist (where the center of AOM should be) should be 163 mm, and beam diameter of around 100 μm was achieved.

2. Mount the mirrors for single pass as well as AOM on the board, and optimize for single pass using a free space power sensor with iris.

3. Place the lens on the board, and slide the lens along the beam path until 0th and 1st order beams are parallel by checking the beam locations with beam profiler. Once the optimal lens position is found, tighten the mounting screw to fix the lens position.

4. Mount the prism and the kinematic mount, and optimize for double pass by placing the power sensor behind the D-shaped mirror and then screwing and unscrewing the prism from the holder and using the knobs of the kinematic mount to maximize for first order optical power.

5. Place the two mirrors for double pass, and optimize for final fiber coupled output power with the mirror mounts and prism holder.

Some remarks on the procedure:

1. The symmetry of the design means that the input and output collimators should have the same focus. This allows them to be adjusted in advance.

2. Step 3 could not be properly done because the mounting holes for the lenses were misplaced and did not allow lenses to be placed one focal length away from AOM. $f = 50$ mm lens was determined to be the best option given the errors in the design and was used for the following measurements.

3. The mounting screw for the prism mount prevents spanner wrench access from the back, so the mount had to be unmounted from the board everytime the prism orientation was to be changed. A different mount that allows changes in prism orientation without taking it off the board may speed up the alignment process.

4. The 0th order beam was blocked using a makeshift setup made out of tape and clamps. A 3D-printed flag could be a more robust permanent solution for the boards.

5. The current collimator holder design is such that the collimators have to be adjusted before it is mounted on the holder. Design could be adjusted such that it allows access to collimator screws, which would allow tuning of output collimator during the last step of assembly for fiber coupling. Currently the prism is adjusted to optimize for both double pass diffraction efficiency and fiber coupling efficiency (steps 4 and 5, and if the focus of output collimator could be tuned while it is mounted, then potentially prism can be used only

for double pass diffraction efficiency and the output collimator focus for the fiber coupling (along with the two mirrors).

6. When optimizing for double-pass efficiency in free-space, you cannot turn the RF on and off to verify that you are indeed measuring the first order diffraction. One way to verify this is by varying the second pass incidence angle by tuning the prism mount and making sure that you can see 0-th and -1 order spots being maximized as you change the angle.

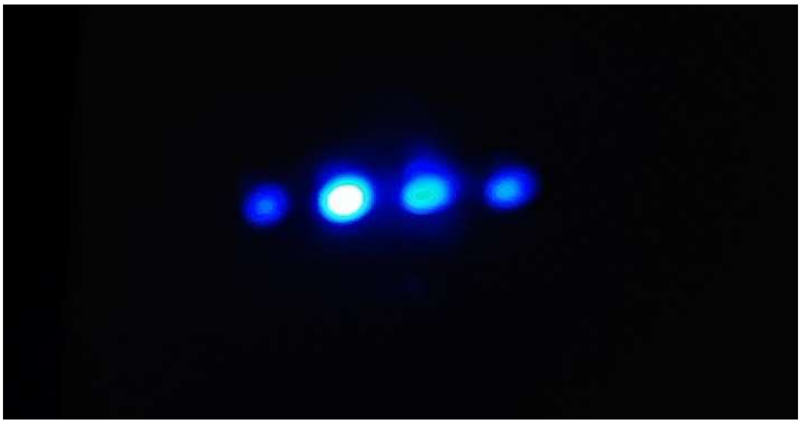

Figure 4.4: Picture of a diffraction pattern of double-passed light on a piece of paper. The brightest spot is from +1 order diffraction. To right of it, we have 0th and -1 order diffraction, and to the left, +2 order. When you see a diffraction similar to this with a piece of paper, you can be more or less confident that you indeed have the maximized first order coming out of the AOM.

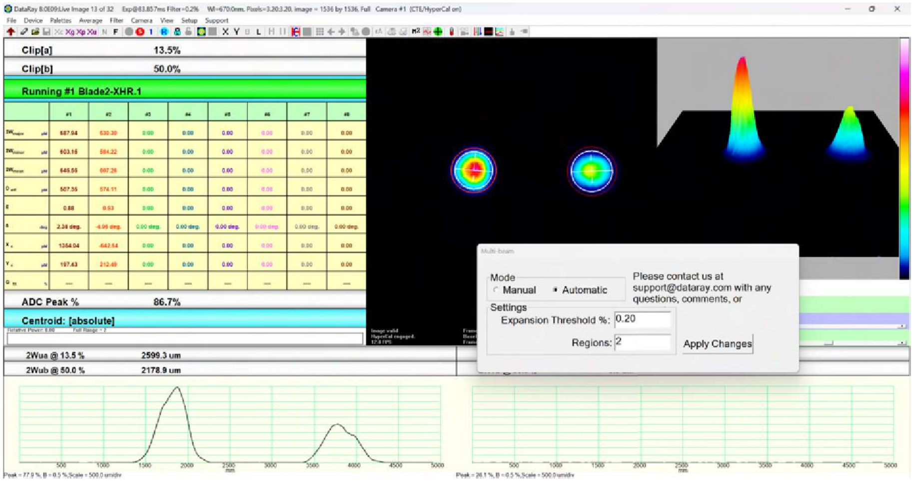

DataRay 8.0E09:Live Image 13 of 32 Exp@83.837ms Filter=0.2% Wl=670.0nm, Pixels=3.20,3.20, image = 1536 by 1536, Full Camera #1 (CTE/HyperCal on)

Clip[a] 13.5%

Clip[b] 50.0%

Running #1 Blade2-XHR.1

	#1	#2	#3	#4	#5	#6	#7	#8
	687.94	630.30	0.00	0.00	0.00	0.00	0.00	0.00
	603.16	584.22	0.00	0.00	0.00	0.00	0.00	0.00
	645.55	607.26	0.00	0.00	0.00	0.00	0.00	0.00
	507.35	574.11	0.00	0.00	0.00	0.00	0.00	0.00
	0.88	0.93	0.00	0.00	0.00	0.00	0.00	0.00
	2.38 deg.	-4.96 deg.	0.00 deg.	0.00 deg.	0.00 deg.	0.00 deg.	0.00 deg.	0.00 deg.
	1364.04	-642.54	0.00	0.00	0.00	0.00	0.00	0.00
	197.43	212.49	0.00	0.00	0.00	0.00	0.00	0.00
	---	---	---	---	---	---	---	---

ADC Peak % 86.7%

Centroid: [absolute]

2Wua @ 13.5 % 2599.3 um

2Wub @ 50.0 % 2178.9 um

Multi-beam

Mode ○ Manual ● Automatic

Please contact us at support@dataray.com with any questions, comments, or

Settings

Expansion Threshold %: 0.20

Regions: 2

Figure 4.5: Screenshot of DataRay software in multi-beam mode. In this mode you can extract parameters from multiple beams, which is convenient during lens position optimization.

4.3 Results

4.3.1 RF power response

First, RF amplitude was swept and diffraction efficiency measured in free space. At 200 MHz, diffraction efficiency of 53 % at 3.4 W was measured, which is close to the expected efficiency of $0.75^2 = 0.56$.

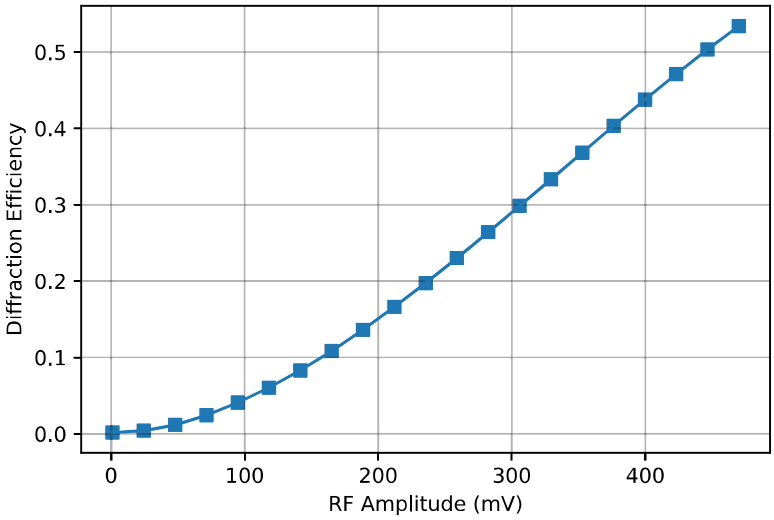

Figure 4.6: Plot of double-passed efficiency against RF amplitude. Note that the response is plotted with RF amplitude this time, not power, which is why the shape of the curve is different. At maximum amplitude shown on the plot, the corresponding RF power is 3.4 W and diffraction efficiency similar to the expected value of $0.75^2 = 0.56$ was observed.

4.3.2 RF frequency response

Next, RF frequency was swept and diffraction efficiency measured in both free space and fiber, and fiber coupling efficiency was calculated as a function of frequency. In free space, efficiency of 53 % was measured at 200 MHz and 3.4 W. Fiber coupled, diffraction efficiency of 36 % was measured, and therefore a fiber coupling efficiency of 68 %. RF frequency bandwidth of 140 MHz was observed.

Fiber coupling efficiency plot for single-pass was super-imposed with the double-pass plot for better comparison. Bandwidth gain by factor of 2 was observed, and this is due to second pass cancelling out the deflection angle from the first pass. Note that the effective bandwidth for the double pass board is twice the bandwidth shown here since the light is passed twice through the AOM so the frequency is shifted by twice the RF frequency, so another factor of 2 is gained in bandwidth just by the virtue of using a double-pass configuration.

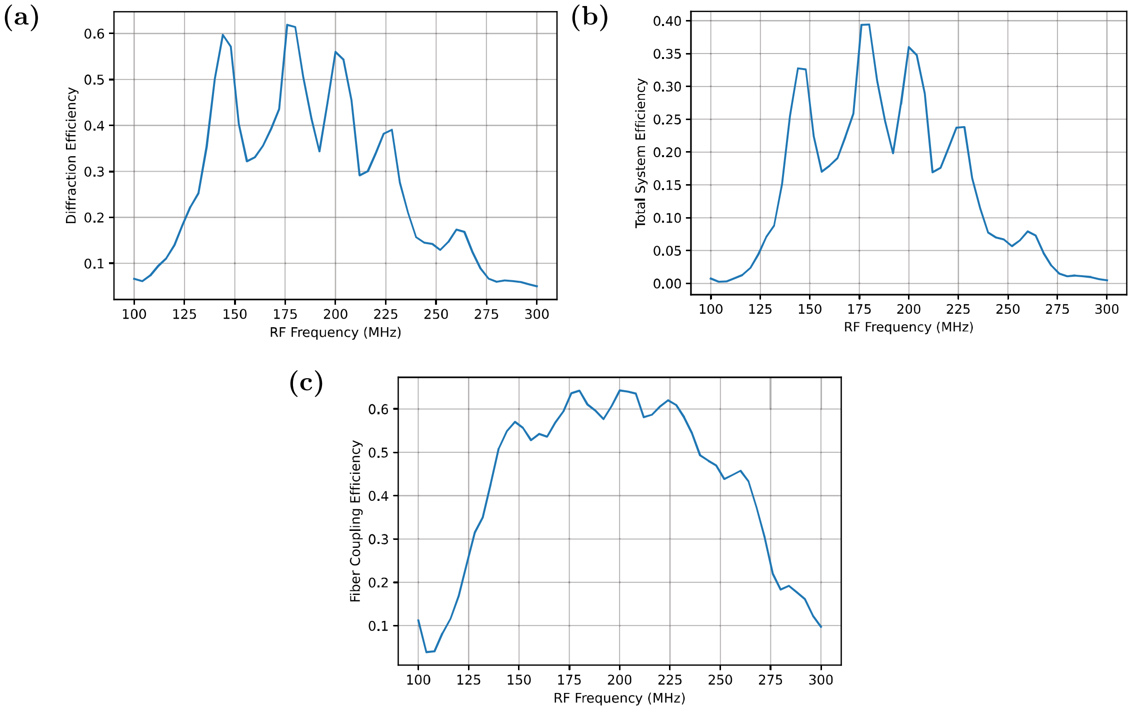

Figure 4.7: (a) RF response of double-pass board in free space. (b) RF response of double-pass board in fiber. (c) Fiber coupling efficiency extract from (a) and (b).

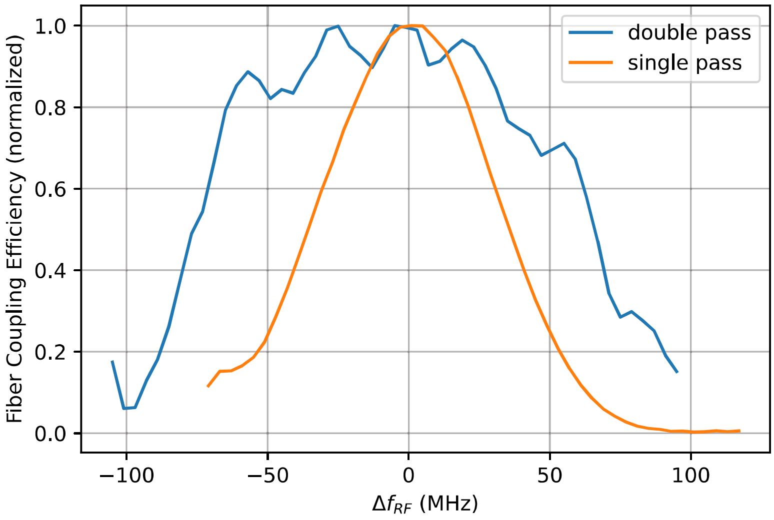

Figure 4.8: Fiber coupling efficiency of single-pass and double-pass system are plotted together to visualize improvement in RF frequency bandwidth. The improvement comes from compensation of the deflection angle during the second pass.

4.3.3 Extinction ratio

As noted in chapter 2, extinction ratio is critical for double-pass boards. When RF is turned off, no optical power was measured with power sensor with minimum power of 1 nW, so extinction ratio of at least 70 dB is achieved with the current board and the makeshift 0-th order block. Extinction ratio could potentially be further improved using a proper 3-printed flag. The flag could also potentially have a hole in the middle such that only first order beam passes through the hole while all the other orders are blocked, as opposed to blocking only the 0th order beam.

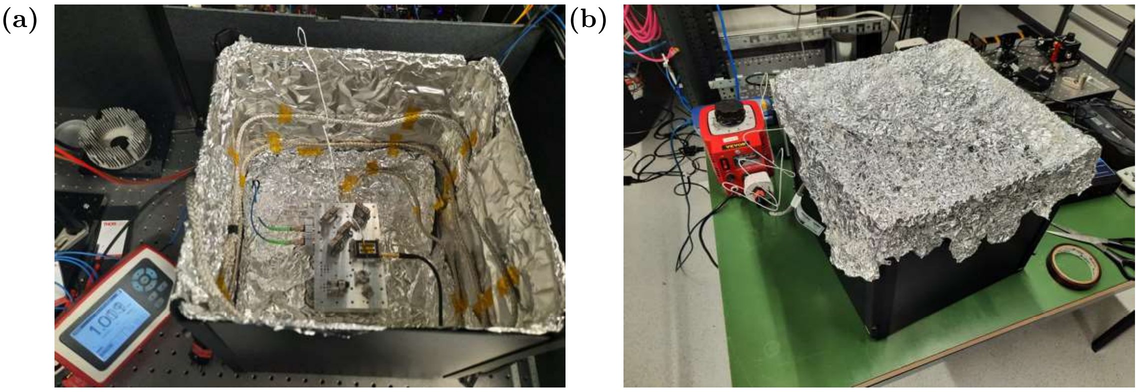

Figure 4.9: (a) Picture of the double-pass board inside the box used for stability measurement. (b) The box was covered with lid also made with aluminum foil during the temperature cycling / drift measurements.

4.3.4 Stability measurement

Lastly, the board was put into a temperature controlled box for stability test under different temperature conditions. The walls of the box were made of 4 aluminum oxide panels with joiner plates for the corners. The box was covered from the inside with aluminum foil to thermally insulate the box from the outside. Heating cord was wrapped around inside the box and sticked onto the aluminum walls with heat resistant tape. The cord was then connected to a transformer with variable voltage level, which was in turn connected to a WiFi connected switch which was automatically turned on and off using a smartphone App. The temperature was recorded using a type-K thermocouple connected to a data logger. A continuously running Python script performed a frequency sweep (similar to ones performed in chapter 3) every 10 seconds and recorded the output optical power out of the board. To calculate the diffraction efficiency, the recorded output power was divided by input optical power shortly before the temperature cycling started.

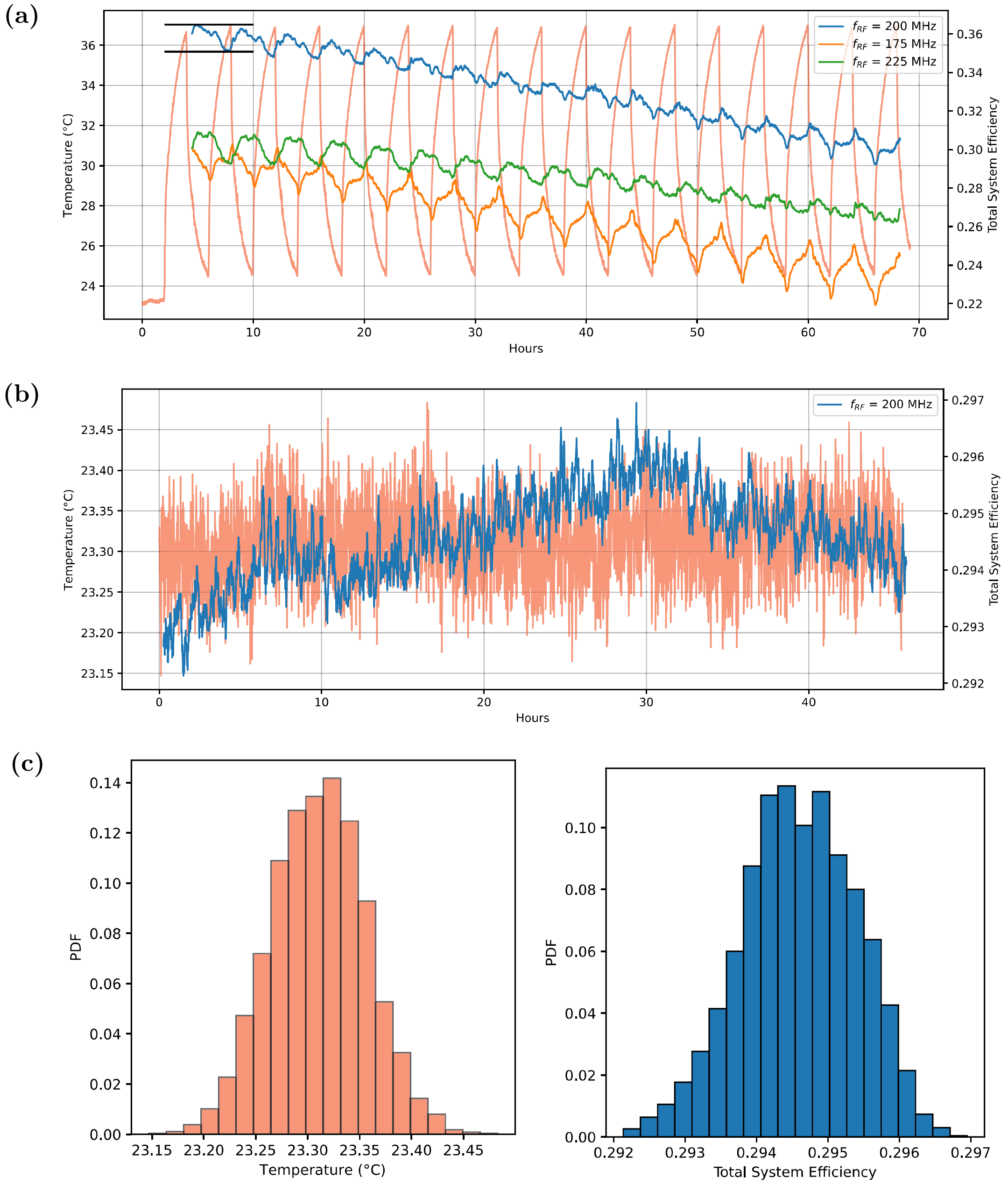

Figure 4.10: (a) Temperature cycling plot. Diffraction efficiency at three different frequencies are plotted against time. The red line is temperature. Two black horizontal lines indicate max diffraction efficiency swing after one temperature cycle. (b) Time series of drift measurement. (c) Probability density distributions of temperature and diffraction efficiency.

The WiFi switch was turned on and off every 2 hours. With the voltage level of 195 V for the transformer, the temperature varied from 24 °C to 36 °C. After one temperature cycle, maximum system efficiency change at $f_{RF} = 200$ MHz was found to be about 4 % relative to the initial efficiency. Over the course of about 70 hours, diffraction efficiency at $f_{RF} = 200$ MHz was reduced by 10 %.

Temperature cycling was then turned off and drift in diffraction efficiency was recorded for another 45 hours to test the stability under normal lab conditions. Mean system efficiency of 29.46 % with standard deviation of 0.80 % was recorded under mean temperature of 23.31 °C with standard deviation of 0.05 °C.

Chapter 5

Conclusion and outlook

A compact and modular double-pass AOM board was assembled and characterized. Peak total system efficiency, including free-space double pass and fiber coupling efficiency, of 36 % at RF frequency of 200 MHz and RF power of 3.4 W was achieved, with effective 3-dB bandwidth of 200 MHz and extinction ratio of > 70 dB. Assembly procedure for the board and potential design improvements were made during the measurement process. Unexpected multiple peak pattern was observed for diffraction efficiency versus RF frequency measurements but the source could not be determined during the project. Temperature cycling measurement demonstrated good resistance to temperature fluctuations; 10 % drop in output power subject to $\pm$ 6 C$^\circ$ of temperature fluctuations for over 3 days.

Appendix A

Appendix

A.1 Output power variations of RF sources

While performing the RF frequency response measurements, change in output power with frequency was observed for both RF sources, without changing the set amplitude. This had a slight impact on the shape of the frequency response curves in chapter 3 and 4. Since the AOM was driven near saturation, the change in power was not taken into account while taking the data.

For the plots below, the power was measured with a hand-held RF power meter, with attenuators to make sure the power doesn't exceed the maximum power rated for the power meter.

A.1.1 Artiq DDS with RF booster

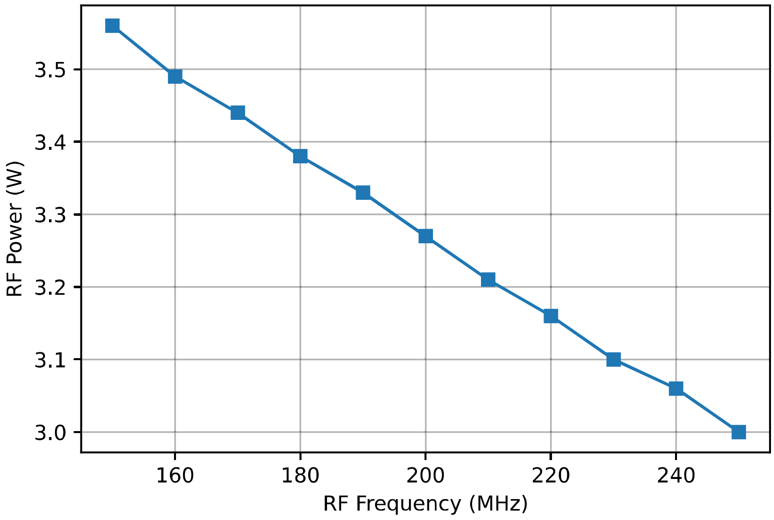

A.1.2 Moku

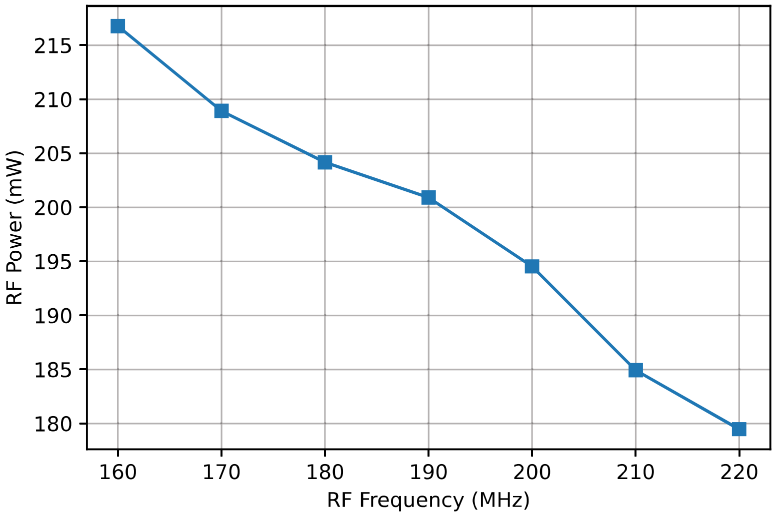

A.2 PM fiber setup

Polarization-maintaining (PM) fibers were used to deliver the light in and out of the double-pass board. The optical power of light delivered from the laser rack to the board sometimes started to fluctuate (after someone has worked on the rack or after a power outage, for example) and the fiber coupling at the laser rack had to be adjusted such that the light is being properly injected into the PM fiber.

The procedure for re-injecting the light into PM fiber is straight-forward. First, improve the fiber coupling if necessary by adjusting the knobs that control the tilt in x, y directions, as well as the focus of the light going into the fiber. Then, connect a polarization analyzer on the other end of the fiber. The polarization analyzer comes with a software that plots the measured polarization on a Poincare sphere. Click on "PER measurement" in the software which will start recording the change in polarization for a few seconds and plot the result on a Poincare sphere. As soon as the software starts recording, move around and bend the fiber such that if the polarization is not properly aligned, the output polarization fluctuates. When the "PER measurement" finishes, the software uses the recorded polarization changes to fit an optimal point on the Poincare sphere where the changes due to mechanical stress on the fiber will be minimal. You can then use the waveplates in the rack to move towards the optimal polarization; it is helpful to look at "adjustment quality" bar in the software which indicates how close you are to the optimal polarization. It also helps to iterate the PER measurement and waveplate adjustments a few times.

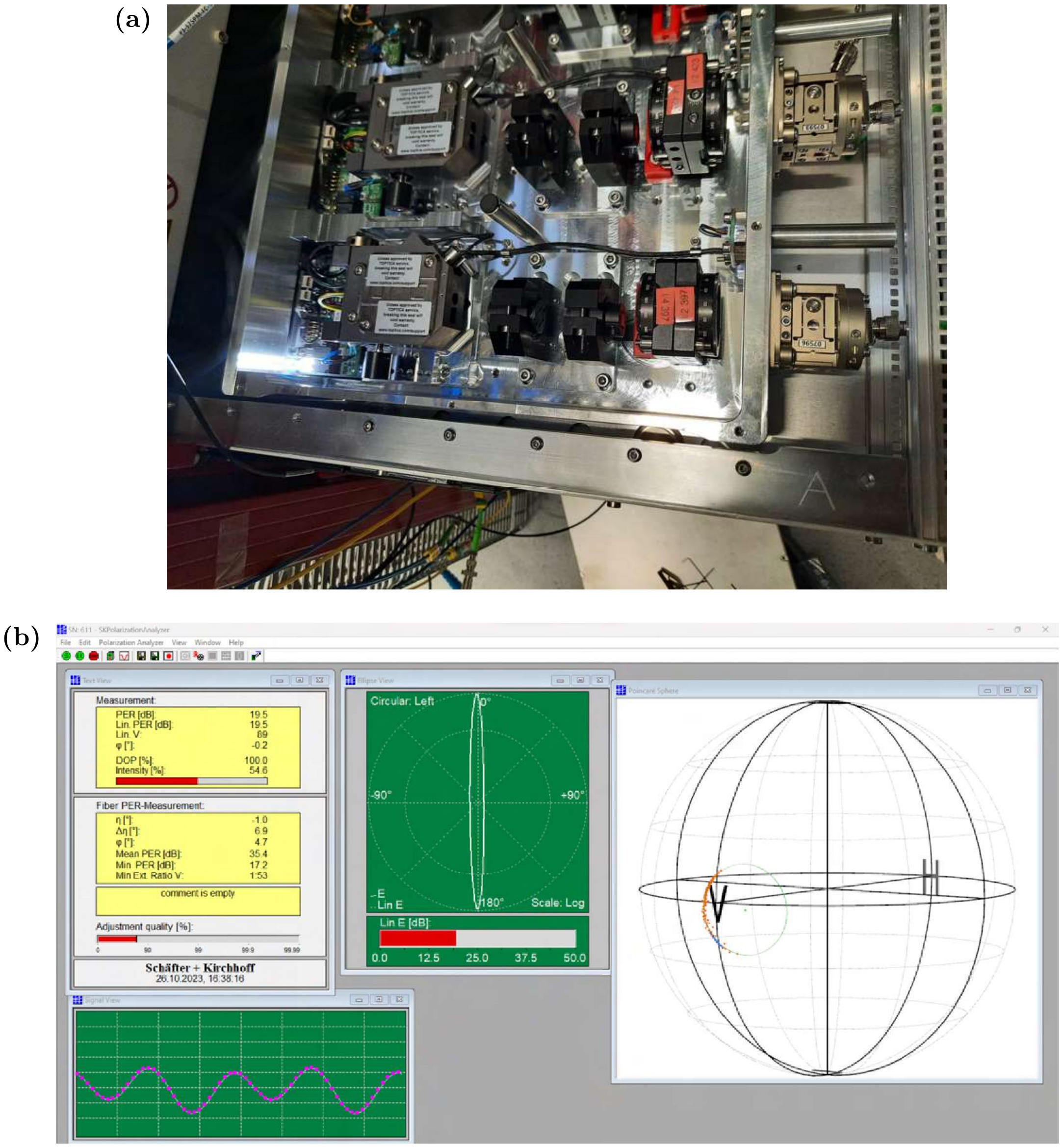

Measurement:
PER [dB]: 19.5
Lin. PER [dB]: 19.5
Lin. V: 89
φ [°]: -0.2
DOP [%]: 100.0
Intensity [%]: 54.6

Fiber PER-Measurement:
η [°]: -1.0
Δη [°]: 6.9
φ [°]: 4.7
Mean PER [dB]: 35.4
Min. PER [dB]: 17.2
Min Ext. Ratio V: 1:53

comment is empty

Adjustment quality [%]:

Schäfter + Kirchhoff
26.10.2023, 16:38:16

Figure A.1: (a) Picture of the laser rack. Box on the left is where the actual laser diode is located. The beam then goes through an optical isolator to prevent any light going back to the laser. The quarter-wave and half-wave plates are labelled with orange stickers. The silver part houses the lens which you can adjust using the knobs on the sides to maximize fiber coupling. (b) Software that comes with polarization analyzer from S&K. Polarizations recorded during "PER measurement" are shown on the sphere, and the points are fitted to find the optimal polarization for the fiber.

A.3 Optics glue-in procedure

Figure A.2: Picture of the optics glue-in setup. The UV-curing light controller shown on the left is connected to a LED pen which outputs the curing light and a foot pedal (not shown in the picture) which one can press down to turn on the light.

Mirrors, both regular and D-shaped, and lenses used for the double-pass board were glued into optical mounts at the beginning of the project. The procedure used for the glue-in is as follows.

1. Wear gloves throughout the procedure to prevent the adhesive from touching your hands and your hands from touching the optics.
2. Prepare a small amount of UV-curing optical adhesive (Thorlabs, NOA61) in an aluminum-foil well.
3. Using a tip of a cable tie, sparingly apply the adhesive on the glue plane of the mount where the optics will make contact.
4. Press down the optics against the glue plane of the mount, and place the mounts down such that the optics do not slide around inside the mount. I used some clamps I found to prop the mounts at an angle.
5. While wearing UV protective goggles, apply UV light (OmniCure, LX500) onto the adhesive. Depending on the type of coating on the optics, they may reflect the curing light away from the adhesive and it may help to apply the

light from the side with no reflective coating such that the light makes it all the way through to the glue. About 10 seconds for each mount is sufficient to cure the adhesive.

6. Do a quick check by shaking the mount and making sure the optics do not fall out / by tapping gently on the mount.

A.4 AOM data sheet

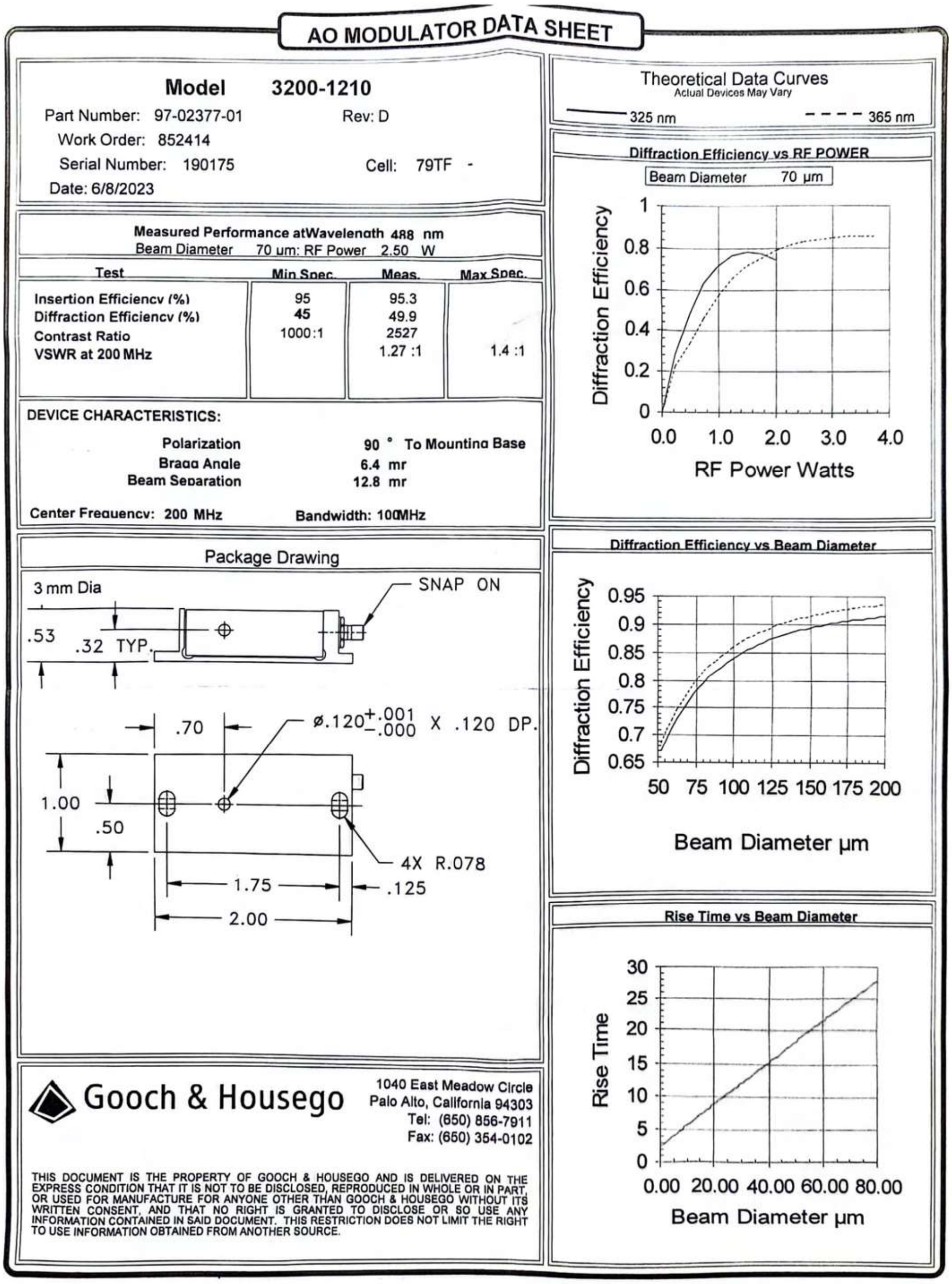

AO MODULATOR DATA SHEET

Model **3200-1210**

Part Number: 97-02377-01 Rev: D
Work Order: 852414
Serial Number: 190175 Cell: 79TF -
Date: 6/8/2023

Measured Performance at Wavelength 488 nm
Beam Diameter 70 um: RF Power 2.50 W

Test	Min Spec.	Meas.	Max Spec.
Insertion Efficiency (%)	95	95.3	
Diffraction Efficiency (%)	**45**	49.9	
Contrast Ratio	1000:1	2527	
VSWR at 200 MHz		1.27 :1	1.4 :1

DEVICE CHARACTERISTICS:

Polarization	**90 ° To Mounting Base**
Bragg Angle	**6.4 mr**
Beam Separation	**12.8 mr**

Center Frequency: 200 MHz **Bandwidth: 100MHz**

Package Drawing

Theoretical Data Curves
Actual Devices May Vary
325 nm 365 nm

Diffraction Efficiency vs RF POWER
Beam Diameter 70 µm

Diffraction Efficiency vs Beam Diameter

Rise Time vs Beam Diameter

Gooch & Housego
1040 East Meadow Circle
Palo Alto, California 94303
Tel: (650) 856-7911
Fax: (650) 354-0102

Bibliography

[1] Donley, E. A., Heavner, T. P., Levi, F., Tataw, M. O., and Jefferts, S. R. (2005). Double-pass acousto-optic modulator system. *Review of Scientific Instruments*, 76.

[2] Ghatak, A. K. and Thyagarajan, K. (1989). *Optical Electronics.* Cambridge University Press.

[3] Liu, J. M. (2005). *Photonic Devices.* Cambridge University Press.

[4] Malinowski, M. (2021). *Unitary and Dissipative Trapped-Ion Entanglement Using Integrated Optics.* PhD thesis, ETH Zurich.